Satellite-based assessment of methane emissions from the Darvaza gas crater

Adriana Valverde[1*], Itziar Irakulis-Loitxate[2,1], Javier Gorroño[1], Zhipeng Pei[3] and Luis Guanter[1,4]

[1] Research Institute of Water and Environmental Engineering (IIAMA), Universitat Politècnica de València, Spain

[2] International Methane Emission Observatory (IMEO), United Nations Environment Programme, Paris, France

[3] State Key Laboratory of Information Engineering in Surveying, Mapping and Remote Sensing, Wuhan University, Wuhan, China

[4] Environmental Defense Fund, Amsterdam, Netherlands

* Corresponding author's email: avaligl@doctor.upv.es

Abstract

Methane (CH_4) is one of the most potent greenhouse gases, and the gas-burning Darvaza crater in Turkmenistan is a rare and persistent emitter. There are substantial uncertainties regarding the date of the crater formation (assumed to be either in 1963 or 1971), the ignition of the fire, and the relation between the fire intensity and methane release. In this study, we reconstruct the fire history using historical Landsat imagery, identifying that combustion began between late 1987 and early 1988. To quantify current methane emissions, we used hyperspectral satellites (EnMAP, PRISMA, EMIT, GF-5A, and ZY-1E) to detect 44 methane plumes between 2020 and 2025, with emission rates ranging from 1,000 to 3,000 kg/h. These observations indicate annual emissions of several thousand tonnes, and over these five years, we estimate a total of 71 ± 21 kt of CH_4. Extrapolating this annual amount since the crater's formation suggests total emissions above 900 ± 300 kt. Additionally, temporal analysis reveals a gradual decline in flaring intensity, although no apparent correlation with methane release was identified. This integrated analysis reduces key uncertainties about the origin and behavior of the Darvaza crater and contributes to a better understanding of long-term natural-anthropogenic methane emissions and their environmental implications.

Keywords

Methane emissions, Darvaza, crater, gas combustion, time series, hyperspectral satellites, fire radiative power, Turkmenistan

Introduction

Methane (CH_4), the primary component of natural gas -comprising approximately 77–99% by volume (1)- is a short-lived but highly potent greenhouse gas. Its global warming potential is approximately 80 times greater than carbon dioxide (CO_2) over a 20-year timeframe (2, 3). The observed increase in atmospheric methane is partly driven by oil and gas exploration, production, and transportation emissions, particularly from leaks, venting, and inefficient flaring across the supply chain (4). This growing concern over methane emissions is particularly relevant in areas with significant natural gas resources.

One such region, the Amu Darya Basin (ADB; Figure 1), in central and eastern Turkmenistan, is a zone of exceptional geological and petroleum significance. Renowned for its abundant oil and gas reserves, the basin extends over 417,000 km^2 and has accumulated nearly 15 km of sedimentary deposits since the Paleozoic era (5). This region's unique geology has multiple structural and stratigraphic traps facilitating the accumulation of oil and gas reserves. Although extensively explored for its petroleum systems, the ADB exhibits a clear predominance of gas-prone characteristics, with gas fields present throughout all main structural zones, whereas oil discoveries have been restricted to a few small fields (5, 6). Specifically, reserve modeling suggests that the total undiscovered resources are estimated at approximately 3.31 billion tons, with gas comprising more than 98% (7). Within the broader context of the ADB, the Karakum High in the northwestern Karakum Desert contains anticlinal folds and faults forming structural traps for hydrocarbon accumulation. Notably, around 20 gas fields have been discovered in this area (6). This rich hydrocarbon province has attracted extensive exploration since the Soviet period, including sulfur works active until the 1960s (8), adding to its complex environmental profile.

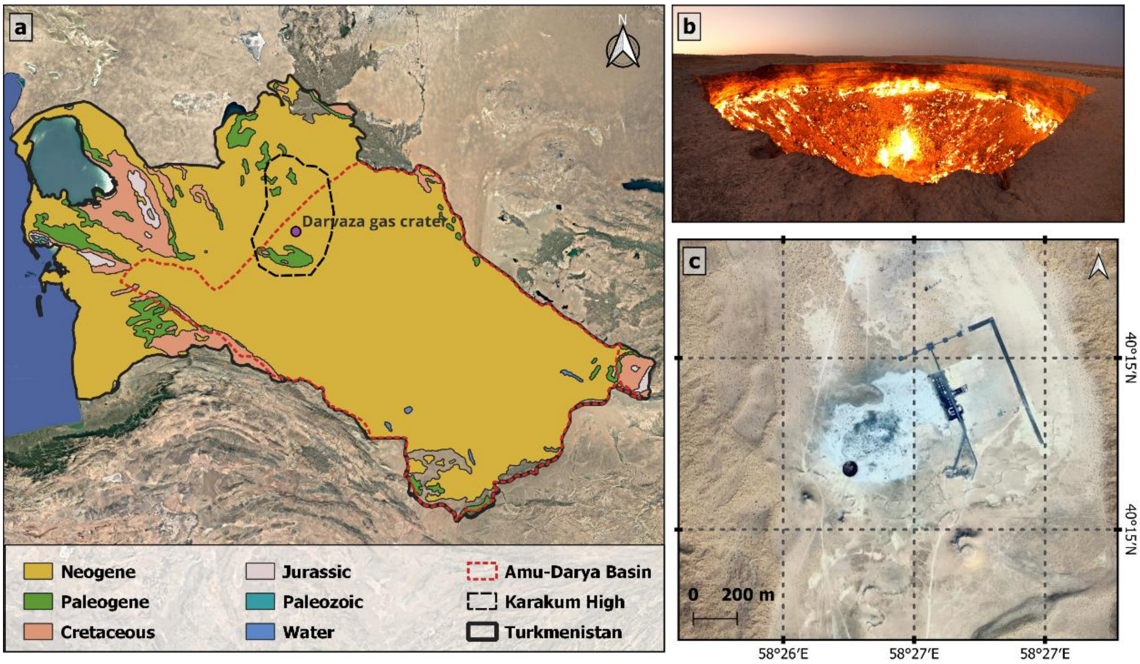

Figure 1.a) Geological map of Turkmenistan showing the location of Darvaza gas crater (purple dot). Map background: Google Satellite. Data source: (9). b) Ground-level view of the burning Darvaza gas crater. Image: (10). c) A satellite image of the crater area from Google Satellite shows local infrastructure.

The Darvaza gas crater, popularly known as the "Door to Hell", represents a relevant case of interaction between natural processes and anthropogenic activity. According to some studies, the crater's formation can be traced back to 1963, when drilling at the Chaljulba structure of the Zeagli–Derweze field uncovered a gas-filled void, leading to the collapse of the overlying sediments, released a large quantity of methane (11, 12). Conversely, other accounts attribute the crater's creation to an incident in 1971 (13–15). In either case, a crater was formed approximately 30 meters deep and 60-70 meters in diameter (see Figure S1). Years later, geologists ignited the escaping gas to mitigate the associated hazard, and it has continued to burn for decades, persisting to the present day (7). Some previous studies have estimated that total methane from the Darvaza crater may have reached approximately 3,796 kt CH_4 over the last 50 years (13). Notably, in this estimate, it is assumed that all of the released methane undergoes complete combustion in the crater fire, rather than being directly vented into the atmosphere. These estimates are based on indirect methods and carry considerable uncertainty, particularly regarding the temporal dynamics of emissions. Additionally, recent estimates (12) suggest the actual flux of methane through the crater is roughly 2.3 t CH_4 per hour, with only ~70% combustion efficiency, meaning that approximately 1.6 t/h is burned, and 0.7 t/h is emitted directly. However, these studies use indirect measures such as flaring to calculate methane estimates.

Given that previous assessments of methane emissions have been based on indirect methods, this study aims to detect and quantify the emissions released over the years since the crater's formation using direct satellite observations. Specifically, we employ both hyperspectral and multispectral satellite data to identify and monitor methane plumes. Hyperspectral sensors, due to their high spectral resolution, can detect absorption features specific to methane in the shortwave infrared (SWIR) region, making them well-suited for detecting emission sources. In parallel, multispectral imagery is used to support the temporal reconstruction of key events, such as refining the ignition date of the crater. Although multispectral sensors lack the spectral resolution required to detect weak methane signals, their extensive long-term archives are critical for historical analysis, offering a unique opportunity to reconstruct environmental processes retrospectively over decades (16). By integrating these datasets, we assess the volume of methane emitted and explore its potential correlation with the ongoing fire. Additionally, the study refines the estimation of the crater's ignition date, which is essential for understanding the temporal scale of its environmental impact. This multi-sensor approach demonstrates the capability of satellite remote sensing to support the identification and monitoring of methane emissions in remote regions with limited ground-based observations, such as the Darvaza gas crater.

Materials and Methods

Reconstruction of the crater origin and fire onset from historical Landsat data

To investigate the origin of the crater and the onset of the persistent fire, we began by analyzing historical satellite imagery from the Landsat program, which has been in operation since 1972. The early missions, Landsat 1–3, were equipped with the MSS sensor, which captures four-band images in the visible and near-infrared (NIR) spectrum at a resolution of 57 × 79 meters (resampled to 60 meters in the Landsat Collection 1 Archive). Later missions, Landsat 4–5, carried both the MSS and the TM sensor, which offers seven spectral bands at a higher spatial resolution of 30 meters, and includes thermal and SWIR bands necessary for fire detection, which were unavailable in Landsat 1–3 (17). For this study, we obtained the data from the USGS Earth Explorer (18) , specifically the Landsat 4-

5 TM C2 L1 Collection (19) and focused our analysis on band 7 (SWIR-2, 2.08–2.35 µm) and thermal band 6 (10.4–12.5 µm) from each acquisition (see Figure S2).

Flaring activity from Fire Information for Resource Management System (FIRMS)

In this study, we used Fire Radiative Power (FRP) data to monitor the intensity of combustion and flaring activity, as it directly measures the radiant energy emitted by fires, making it a key parameter for monitoring flaring events. FRP data was obtained from the Fire Information for Resource Management System (FIRMS) platform, which provides daily observations from the VIIRS sensors onboard the Suomi NPP and NOAA-20 satellites (20). These data offer diurnal and nocturnal observations at a spatial resolution of 375 m from 2012 to the present. The FIRMS data were downloaded from the NASA FIRMS Archive Download (21). In addition, despite its lower sensitivity but given its long historical record, MODIS (Moderate Resolution Imaging Spectroradiometer) data were also downloaded from the FIRMS archive, with MODIS C6.1 data available from November 2000 (for Terra). MODIS provides daily (day and night) global active fire data at 1 km pixel resolution (22). See more information in the SI.

Detection and quantification of methane plumes from hyperspectral data

We have analyzed a dataset composed exclusively of hyperspectral satellite imagery to detect and quantify the methane emissions from the Darvaza gas crater. The combination of surface heterogeneity and the intensity of the emissions, together with the fire signal in the source, makes methane detection by multispectral satellites challenging.

We have obtained 61 images from different instruments (see Table S1). Specifically, the dataset includes 9 from the Advanced Hyperspectral Imager (AHSI) on the Ziyuan-1 (ZY-1E) satellite, 2 from the AHSI on China's Gaofen-5A (GF-5A) satellite, 13 from PRISMA, 9 from EnMAP, and 14 from the EMIT instrument onboard the International Space Station (ISS). These instruments offer high spectral resolution in the SWIR region, including the 1700 nm and 2300 nm spectral windows where methane exhibits distinct absorption features suitable for remote detection and quantification.

EnMAP, PRISMA, and EMIT have demonstrated strong capabilities for methane emission detection, supported by their spectral coverage in the SWIR (23–25). These instruments combine suitable spectral resolution with moderate spatial sampling (30 m for EnMAP and PRISMA; 60 m for EMIT), enabling reliable plume identification. However, the availability of data from those missions is low due to their sparse spatio-temporal sampling. Our dataset was also obtained from two versions of the AHSI instruments onboard China's GF-5A and ZY-1E satellites (26–28) . These hyperspectral platforms provide moderate spatial resolution and wide swath coverage, making them ideal for regional assessments, although their signal-to-noise ratio and radiometric calibration may limit precise emission detection.

Estimation of total methane emissions

We derived methane concentration enhancement (ΔXCH_4) maps from the hyperspectral L1B radiance data using a matched-filter retrieval algorithm (29) adapted to each sensor's spectral configuration. Visual inspections of the resulting ΔXCH_4 maps were conducted to identify plume-like structures. These were then cross-referenced with high-resolution base maps from Google Earth to exclude retrieval artifacts and confirm the source of the plume. Additionally, we verify the coherence between observed plume orientation and the wind speed at 10 m above the surface (U10) derived from the NASA Goddard Earth Observing System-Fast Processing (GEOS-FP) meteorological reanalysis product (30). The GEOS-FP

U10 product has a temporal resolution of 1 hour. In our analysis, wind data were linearly interpolated between the nearest hourly values. A comparison between GEOS-FP and ERA5-Land wind data (31) (Figures S3–S4) showed that the differences did not significantly affect the emission estimates. Finally, we applied the Integrated Methane Enhancement (IME) method to quantify methane emissions, translating column concentration into emission fluxes (32, 33). Finally, to estimate total emissions over the 2020–2025 period, we fit a second-degree polynomial to the time series of flux estimates and integrated the resulting curve. Uncertainty in the total emission estimate was assessed via Monte Carlo simulations.

Results and Discussion

Reconstructing the history of the crater using historical satellite observations

There has been ongoing disagreement in the literature regarding the formation date of the crater. Various sources report differing dates for the crater's formation, with some indicating 1963 (11, 12) and others suggesting 1971 (13–15). What can be conclusively established is that the crater was already present by October 25, 1972, based on the analysis of a Landsat 1 image, which clearly shows the crater. However, the exact year of its formation remains uncertain, and it is not possible to determine whether the crater was formed shortly before this date or significantly earlier.

To approximate the onset of flaring activity at the Darvaza gas crater, an essential factor in determining whether methane emissions were combusted or directly emitted, we conducted an analysis of satellite imagery from the Landsat 4–5 Thematic Mapper (TM) missions covering the period 1984–1988. Notably, thermal data from Band 6 (thermal infrared – TIR) and Band 7 revealed no sustained thermal anomalies indicative of active flaring between 1984 and early 1988. This absence of thermal signatures persisted until a change was observed between September 1987 and February 1988, when the onset of flaring was detected (Figure 2). This finding, which provides the first temporal constraint on the ignition of the crater, refines previous estimates suggesting that burning may not have begun until the 1980s (34). Since that point, the crater has burned continuously, exhibiting combustion behavior similar to industrial gas flaring, but unlike typical flares, it is not static. The crater, approximately 60–70 meters in diameter, exhibits dynamic flame movement along various surface fissures and vents within the cavity (see Figure 2). The subsurface comprises alternating sedimentary layers, aquifers, and denser formations that may facilitate sustained gas migration toward the surface (7), suggesting that emissions may not originate from a single reservoir but from multiple subsurface gas sources contributing to persistent combustion. In this context, the onset of flaring represents not only a visible transformation of the crater but also a critical shift in its emission behavior; in the absence of combustion, the gas, primarily methane, would likely have been released directly into the atmosphere, resulting in substantially higher.

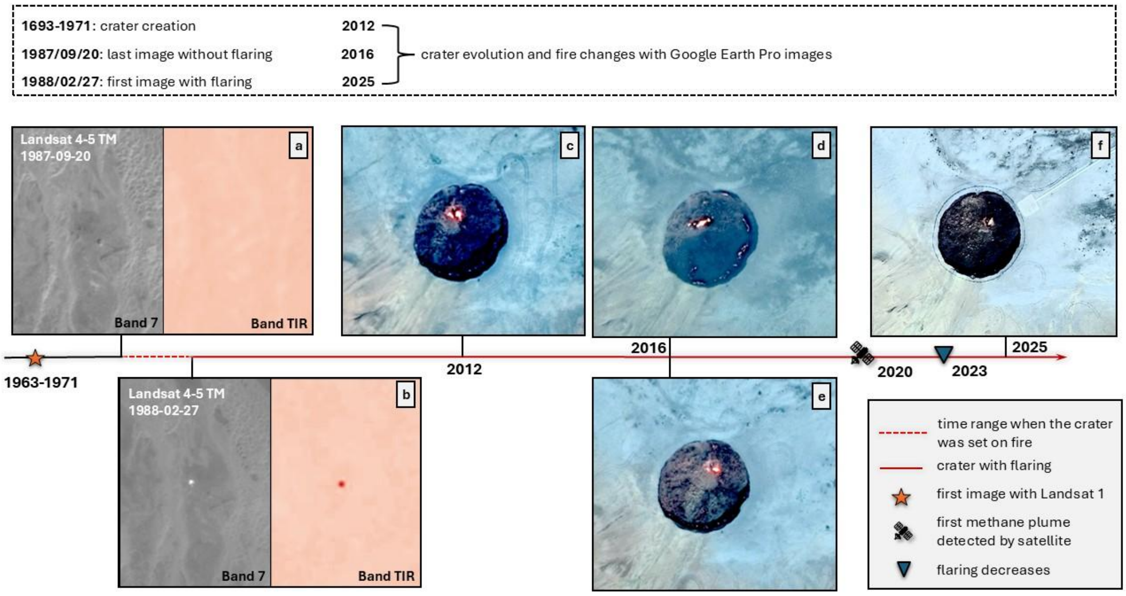

Figure 2. The timeline of the Darvaza gas crater is based on satellite observations. The top section summarizes key events: crater formation (1963 or 1971), the last satellite image without flaring (1987/09/20), and the first image showing flaring (1988/02/27), and from 2012 to 2025, the crater's evolution and fire activity were monitored using Google Earth Pro high-resolution imagery. Panels (a) and (b) show Landsat 5 TM images, with Band 7 in grayscale and Band 6 (thermal infrared) in orange tones; thermal activity is absent in 1987 but clearly visible in 1988. Panels (c) through (f) depict the crater's evolution and varying fire intensity from 2012 to 2025 ((c), (d), (e) images © Maxar Technologies; (f) image © 2025 Airbus). Symbols in the bottom right legend mark key events: the first Landsat detection (1971), the onset of flaring in early 1988, the first satellite-based methane plume detection (2020), and a visible decrease in flaring activity by 2023.

Detection of methane plumes using hyperspectral satellite data between 2020 and 2025

Owing to the lack of long-term historical hyperspectral satellite records - unlike the extensive archives of multispectral systems such as Landsat - our analysis of methane emissions over Darvaza Crater is limited to recent observations from 2020 onwards. Between April 2020 and May 2025, 44 methane plumes were identified over the Darvaza crater region in Turkmenistan using imagery from various hyperspectral satellite missions. Specifically, 6 plumes were detected by ZY-1E, 2 by GF-5A, 13 by PRISMA, 9 by EnMAP, and 14 by EMIT (see Table S2), the first confirmed detection recorded by ZY-1E in April 2020 (Figure 3), with an emission of 1.8 ± 0.7 t/h. The highest methane emission was detected by ZY-1E on 22 August 2023, with an estimated rate of 3.18 ± 1.20 t/h. This value closely aligns with a subsequent observation by EMIT three days later, which recorded a similar emission rate of 3.16 ± 1.28 t/h, reinforcing the temporal consistency of high-intensity release events. A comparable pattern was observed on 7 November 2024, when PRISMA and EnMAP detected plumes with closely matching magnitudes, 1.14 ± 0.45 t/h and 1.26 ± 0.49 t/h, respectively. Conversely, the lowest emission recorded was 632 ± 230 kg/h, measured by EMIT in July 2024. See the detection time series in Figure 3.

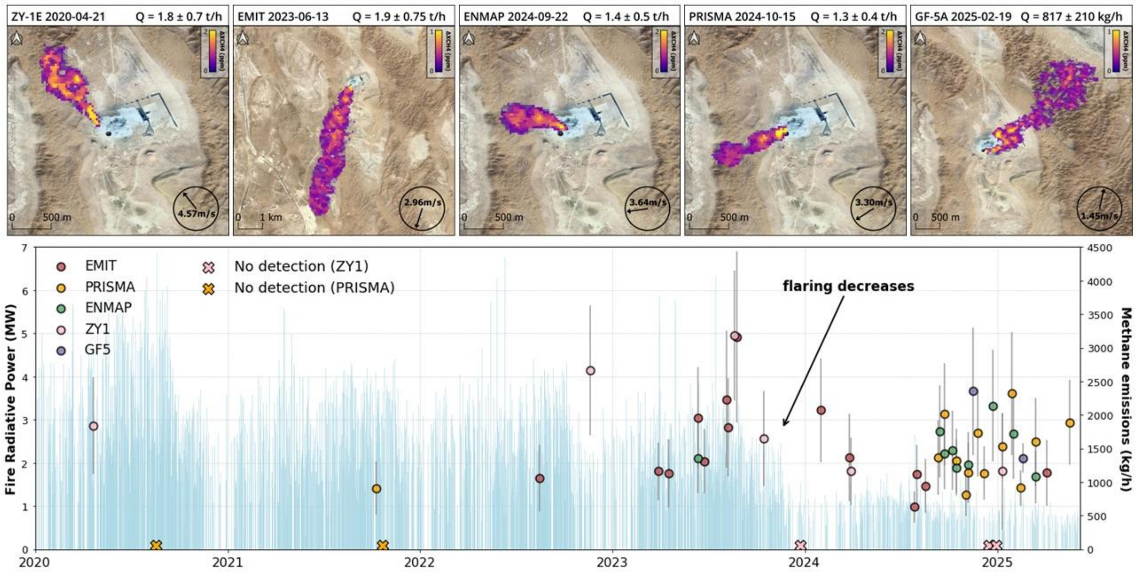

Figure 3. Time series of methane plumes and flaring activity at the Darvarza crater. In the upper panels, examples of methane plumes from different satellites on different dates. Map background: Google Satellite. At the bottom, historical flaring analysis using only VIIRS (26) and the time series of the detected plumes with their emission flux rate estimates and the uncertainty represented as vertical error bars (see Table S2 for more information).

These observations reveal significant variability in emission intensities (from ~0.6 to 3 t/h), consistent with the dynamic nature of gas release from geological features like this crater. Additionally, multiple factors are probably influencing the positive detection of methane plumes. Meteorological variables such as wind speed and direction can significantly alter plume shape, dispersion, and column concentration, thus impacting satellite-based retrievals. Furthermore, it is critical to consider the high frequency of dust storms in the Karakum Desert, which records the highest incidence of dust storms in Central Asia, with more than 40 events annually (7). These dust storms can significantly increase atmospheric aerosol load, introducing additional scattering and absorption in the SWIR spectral region (35). Besides, meteorological conditions such as rainfall or snow cover during winter can significantly affect the surface radiance and the level of the crater's fire, although such weather events are relatively infrequent, occurring on fewer than 40 days per year (36). For these reasons, we highlight that lack of detection does not necessarily indicate the absence of emissions but reflects the complex interplay between source behavior, atmospheric conditions, surface reflectance, and instrumental sensitivity. This complexity is particularly evident in the analysis of certain ZY-1E and PRISMA acquisitions, where no plumes were detected despite the probability of ongoing emissions (see Table S3). The absence of plumes in these 5 images can be attributed to the timing of the acquisitions, which may have been unfavorable for detection. Specifically, one ZY-1E image was captured during strong winds (>11.5 m/s), and several others under relatively high wind conditions.

On the other hand, a reduction in flaring was observed after summer 2023; however, no clear correlation has been found between this reduction and the intensity of methane emissions (see Figure 3). These observations suggest that part of the gas may be released directly into the atmosphere through multiple subsurface fissures, bypassing combustion. While some of the methane is visibly flared, a significant portion may escape unburned due to the complex geological structure of the crater, which probably includes diffuse venting pathways, potentially explaining the lack of correlation between flaring intensity and methane emission.

In parallel with these observations, recent efforts have focused on mitigation through subsurface intervention in response to persistent methane emissions. Specifically, scientists have proposed drilling a well at the Chaldzhulba field to intercept gas-bearing formations between 200 and 950 meters deep to mitigate methane emissions from the crater. This action would allow controlled extraction and gradual gas flow redirection, reducing uncontrolled emissions (12). Early satellite data from Capterio (37) indicates a more than double decrease in visible burning from September 2023, suggesting the effectiveness of the intervention (11, 38). This aligns with our observations (Figure 3), where a noticeable decline in flaring activity is recorded after that period, supporting that the decrease is linked to the mitigation efforts.

Estimation of total emissions from the crater

In our study, we provide a direct assessment based on hyperspectral satellite observations. We interpret the crater's emission history as comprising three distinct periods: (i) 2020–2025, during which methane emissions were directly observed and quantified; (ii) 1988–2019, during which flaring was likely continuous but the methane not directly measured (see Figure S5); and (iii) 1963–1987, when no flaring systems were present and all associated emissions are assumed to have been released as uncombusted methane.

For the most recent period (2020–2025), we estimate total methane emissions of 71 ± 21 kt CH_4 (see Figure S6), based on plume detections using hyperspectral satellite observation. This estimate is currently the most reliable, grounded in direct observational data and would correspond to approximately 6.0 Mt CO_2-equivalent under a 20-year global warming potential (2), underscoring the substantial short-term climate impact of the observed emissions. For context, this emission level is comparable to major accidental releases such as the Aliso Canyon event in California, which released approximately 97 kt CH_4 over four months (39), and the blowout in Kazakhstan, which is estimated at 131 ± 34 kt CH_4 over a period of 6 months (40). Assuming the crater was formed in 1971, and emissions have remained stable, we have extrapolated potential emissions to approximately 800 ± 250 kt CH_4. However, if the formation year is considered to be 1963, a total period of 62 years, this estimate could increase up to 900 ± 300 kt CH_4. Notably, this estimation should be regarded as highly conservative, as emissions during the initial pre-flaring phase were likely substantially higher. Furthermore, this estimate accounts solely for methane emissions and does not include methane that was combusted.

Conclusions

The Darvaza gas crater represents one of the most intriguing natural-anthropogenic geological features globally. Since its formation, estimated in 1963 or 1971, the site has continuously released significant quantities of methane into the atmosphere. The geological configuration of the crater, characterized by alternating sedimentary strata and aquifers, facilitates upward gas migration and persistent emissions originating from multiple subsurface reservoirs.

This study analyzed the history of the crater using the Landsat 1–5 archive, determining that flaring at the crater began between September 1987 and February 1988. This represents a novel finding, as no prior study had established ignition timing with such temporal resolution. This temporal constraint is critical for reconstructing the history of emissions, as it implies that during the pre-flaring period, all methane was vented directly into the atmosphere without combustion. Consequently, emissions during this period would be higher than those recorded during active flaring years.

Furthermore, over the past five years, hyperspectral satellite imagery - including EnMAP, PRISMA, EMIT, GF-5A and ZY-1E - has identified 44 methane plumes above the crater, with emission rates varying from approximately 0.6 to over 3 t/h. Although a reduction in flaring activity was observed during the summer of 2023, no consistent correlation was found between flaring intensity and methane release. This suggests that a substantial fraction of the gas escapes combustion, likely via diffuse or bypassing subsurface venting pathways, and that the proposed activity of drilling wells in nearby fields to reduce the gas flow to the crater would be impacting the amount of gas flared but not the gas vented.

Finally, total methane emissions with direct satellite observations are estimated at 71 ± 21 kt CH_4 for 2020–2025. Extending this analysis to the entire lifetime of the Darvaza crater, we estimate cumulative emissions of at least 800 ± 300 kt CH_4, depending on its year of creation, could have reached 900kt. This value represents a conservative lower bound, as it does not account for potentially higher emissions during the early, pre-flaring decades. These findings underscore the critical value of integrating high-resolution hyperspectral satellite data with historical activity records to constrain persistent methane sources' long-term climate impact accurately. The case of the Darvaza crater exemplifies the potential of Earth observation tools to uncover and quantify emissions from long-lived, poorly monitored sources, highlighting a need to incorporate such features into regional and global methane inventories.

Acknowledgment

We thank the Italian Space Agency (ASI) and the German Aerospace Center (DLR) for facilitating PRISMA and EnMAP acquisitions, respectively. We also acknowledge the team at NASA's Jet Propulsion Laboratory for providing EMIT data and maintaining the Landsat program. In addition, we are grateful to Daniel Varon for supplying the WRF-LES wind simulations used in this study. The authors would like to thank the China Centre for Resources Satellite Data and Application for the GF-5A and ZY-1 data used in this study.

References

1. M.-S. Bahr, M. Wolff, PAS-based isotopologic analysis of highly concentrated methane. *Front. Environ. Chem.* **3**, 1029708 (2022).

2. R. K. Pachauri, L. Mayer, Intergovernmental Panel on Climate Change, Eds., *Climate change 2014: synthesis report* (Intergovernmental Panel on Climate Change, 2015).

3. M. Etminan, G. Myhre, E. J. Highwood, K. P. Shine, Radiative forcing of carbon dioxide, methane, and nitrous oxide: A significant revision of the methane radiative forcing. *Geophysical Research Letters* **43**, 12,614-12,623 (2016).

4. M. Saunois, *et al.*, Global Methane Budget 2000–2020. *Earth Syst. Sci. Data* **17**, 1873–1958 (2025).

5. M.-F. Brunet, *et al.*, Late Palaeozoic and Mesozoic evolution of the Amu Darya Basin (Turkmenistan, Uzbekistan). *Geological Society Publications* **427**, 89–144 (2017).

6. G. F. Ulmishek, Petroleum geology and resources of the Amu-Darya basin, Turkmenistan, Uzbekistan, Afghanistan, and Iran. *USGS Numbered Series* 38 (2004). https://doi.org/10.3133/b2201H.

7. M. R. Ghassemi, E. Garzanti, Geology and geomorphology of Turkmenistan: A review. *Geopersia* **9(1)**, 125–140 (2018).

8. P. Brummell, *Turkmenistan: the Bradt travel guide* (Bradt Travel Guides, 2005).

9. T. D. Drummer, Generalized Geology of the Former Soviet Union (geo1ec). U.S. Geological Survey. https://doi.org/10.5066/P9GUL0PQ. Deposited 1998.

10. T. Sandtorv, Darvasa gas crater panorama [Cropped photograph]. *Wikimedia Commons* (2011). Available at: . https://commons.wikimedia.org/wiki/File:Darvasa_gas_crater_panorama.jpg [Accessed 5 April 2025].

11. B. K. Pirniyazov, I. I. Luryeva, The method of reducing methane emissions from the Derweze crater, proposed by Turkmen scientists, has received practical confirmation. *ORIENT* (2024). Available at: https://orient.tm/en/post/71298/method-reducing-methane-emissions-derweze-crater-proposed-turkmen-scientists-has-received-practical-confirmation.

12. M. Davis, A New Perspective on Old Flames: Satellite Tracking of Emissions Reduction at the 60-Year Darvaza Fire Crater in Turkmenistan. *FlareIntel* (2024). Available at: https://flareintel.com/insights/a-new-perspective-on-old-flames-satellite-tracking-of-emissions-reduction-at-the-60-year-darvaza-fire-crater-in-turkmenistan#_ftn7.

13. J. Duggan, G. Gillan, L. Meehan, A. Tyrrel, P25 The Doorway to Hell. *Physics Special Topics* **19** (2020).

14. S. Vlasov, *et al.*, *Methane in the atmosphere, methanotrophs and development of oil and gas industry* (LLC MAKS Press, 2021).

15. S. A. G. Leroy, R. Gracheva, A. Medvedev, Natural hazards and disasters around the Caspian Sea. *Nat Hazards* **114**, 2435–2478 (2022).

16. T.-L. He, R. J. Boyd, D. J. Varon, A. J. Turner, Increased methane emissions from oil and gas following the Soviet Union's collapse. *Proc. Natl. Acad. Sci. U.S.A.* **121**, e2314600121 (2024).

17. D. P. Roy, *et al.*, Landsat-8: Science and product vision for terrestrial global change research. *Remote Sensing of Environment* **145**, 154–172 (2014).

18. USGS science for a changing world, Earth Explorer. Available at: https://earthexplorer.usgs.gov/ [Accessed 5 January 2025].

19. Earth Resources Observation and Science (EROS) Center, Landsat 4-5 Thematic Mapper Level-1, Collection 2. U.S. Geological Survey. https://doi.org/10.5066/P918ROHC. Deposited 1982.

20. NASA Earthdata, VIIRS (Visible Infrared Imaging Radiometer Suite). (2025). Available at: https://www.earthdata.nasa.gov/data/instruments/viirs.

21. NASA FIRMS, FIRMS fire map: VIIRS active fire data (NOAA-21). *FIRMS Fire Information for Resource Management System* (2025). Available at: https://firms.modaps.eosdis.nasa.gov/map/.

22. NASA, MODIS Standard Collection 6.1 Update. *Atmosphere Discipline Team Imager Products* (2025). Available at: https://atmosphere-imager.gsfc.nasa.gov/documentation/collection-61.

23. L. Guanter, *et al.*, Mapping methane point emissions with the PRISMA spaceborne imaging spectrometer. *Remote Sensing of Environment* **265**, 112671 (2021).

24. A. K. Thorpe, *et al.*, Attribution of individual methane and carbon dioxide emission sources using EMIT observations from space. *Sci. Adv.* **9**, eadh2391 (2023).

25. J. Roger, *et al.*, High-Resolution Methane Mapping With the EnMAP Satellite Imaging Spectroscopy Mission. *IEEE Trans. Geosci. Remote Sensing* **62**, 1–12 (2024).

26. I. Irakulis-Loitxate, *et al.*, Satellite-based survey of extreme methane emissions in the Permian basin. *Sci. Adv.* **7**, eabf4507 (2021).

27. Y.-N. Liu, *et al.*, The Advanced Hyperspectral Imager: Aboard China's GaoFen-5 Satellite. *IEEE Geosci. Remote Sens. Mag.* **7**, 23–32 (2019).

28. L. Yan, J. Li, C. Xiao, Vicarious Radiometric Calibration of the AHSI Instrument Onboard ZY1E on Dunhuang Radiometric Calibration Site. *IEEE Trans. Geosci. Remote Sensing* **60**, 1–13 (2022).

29. D. R. Thompson, *et al.*, Space-based remote imaging spectroscopy of the Aliso Canyon CH_4 superemitter. *Geophysical Research Letters* **43**, 6571–6578 (2016).

30. A. Molod, *et al.*, The GEOS-5 atmospheric general circulation model: mean climate and development from MERRA to fortuna. (2012). Available at: https://portal.nccs.nasa.gov/datashare/gmao/geos-fp/das/.

31. Copernicus Climate Change Service, ERA5-Land hourly data from 1950 to present. Copernicus Climate Change Service (C3S) Climate Data Store (CDS). https://doi.org/10.24381/CDS.E2161BAC. Deposited 2019.

32. C. Frankenberg, *et al.*, Airborne methane remote measurements reveal heavy-tail flux distribution in Four Corners region. *Proc. Natl. Acad. Sci. U.S.A.* **113**, 9734–9739 (2016).

33. D. J. Varon, *et al.*, Quantifying methane point sources from fine-scale satellite observations of atmospheric methane plumes. *Atmos. Meas. Tech.* **11**, 5673–5686 (2018).

34. C. Johnson, What It's Like at the Real-Life 'Gates of Hell' in Turkmenistan. *Mental Floss* (2024). Available at: https://www.mentalfloss.com/posts/turkmenistan-gates-of-hell.

35. H. D. Kambezidis, D. G. Kaskaoutis, Aerosol climatology over four AERONET sites: An overview. *Atmospheric Environment* **42**, 1892–1906 (2008).

36. Weather Atlas, Climate and monthly weather forecast Darvaza, Turkmenistan. (2024). Available at: https://www.weather-atlas.com/en/turkmenistan/darvaza-climate.

37. Capterio, FlareIntel: A digital tool to track and reduce global gas flaring. *FlareIntel*. Available at: https://flareintel.com/.

38. Oilgas, Scientists of Turkmenistan have developed a way to take control of the Darvaza crater. (2022). Available at: https://oilgas.gov.tm/en/posts/habarlar/4895/turkmenistanyn-alymlary-derweze-kraterini-goz-astyna-almagyn-usulyny-islap-duzduler.

39. S. Conley, *et al.*, Methane emissions from the 2015 Aliso Canyon blowout in Los Angeles, CA. *Science* **351**, 1317–1320 (2016).

40. L. Guanter, *et al.*, Multisatellite Data Depicts a Record-Breaking Methane Leak from a Well Blowout. *Environ. Sci. Technol. Lett.* **11**, 825–830 (2024).

Satellite-based assessment of methane emissions from the Darvaza gas crater

SUPPORTING INFORMATION

Adriana Valverde[1], Itziar Irakulis-Loitxate[2,1], Javier Gorroño[1], Zhipeng Pei[3] and Luis Guanter[1,4]

[1] Research Institute of Water and Environmental Engineering (IIAMA), Universitat Politècnica de València, Spain

[2] International Methane Emission Observatory (IMEO), United Nations Environment Programme, Paris, France

[3] State Key Laboratory of Information Engineering in Surveying, Mapping and Remote Sensing, Wuhan University, Wuhan, China

[4] Environmental Defense Fund, Amsterdam, Netherlands

* Corresponding author's email: avaligl@doctor.upv.es

Summary

Number of pages: 7

Tables: S1 to S3

Figures: S1 to S6

The topographic profile was generated using the SRTM 1 arc-second DEM from the USGS, with a spatial resolution of approximately 30 meters. This radar-derived dataset is well-suited for capturing elevation variations, such as the rim and internal depression of the Darvaza gas crater. Its consistent data quality enables a reliable representation of regional geomorphology despite the area's harsh surface conditions. The geological context shown in the plot (Figure S1) is based on the USGS geological map (1), which complements the elevation data by delineating the surrounding sedimentary formations.

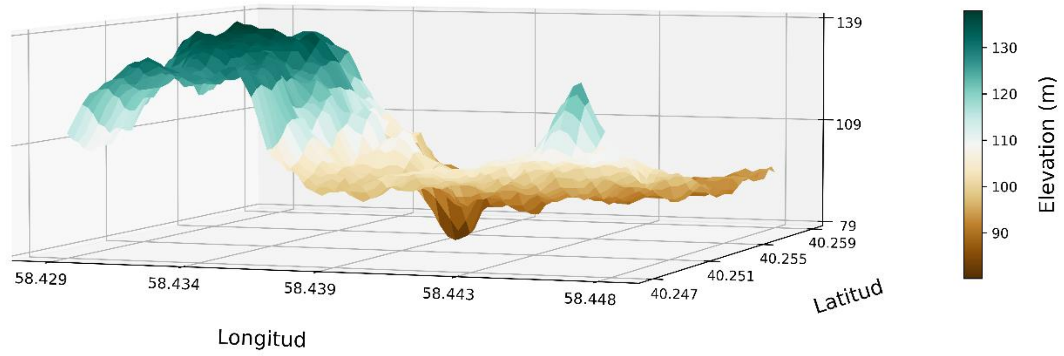

Figure S1. Elevation of the Darvaza gas crater area using the SRTM 1 arc.

In this study, we employed the thermal Band 7 (2.08–2.35 µm) and Band 6 (10.4–12.5 µm) of the Landsat 5 TM to detect and assess flaring activity within the crater (Figure S2). Band 7 was specifically utilized because its spectral range aligns with the peak thermal emission of typical gas flaring temperatures (~1500 K), as described by the Planck radiation law (2).

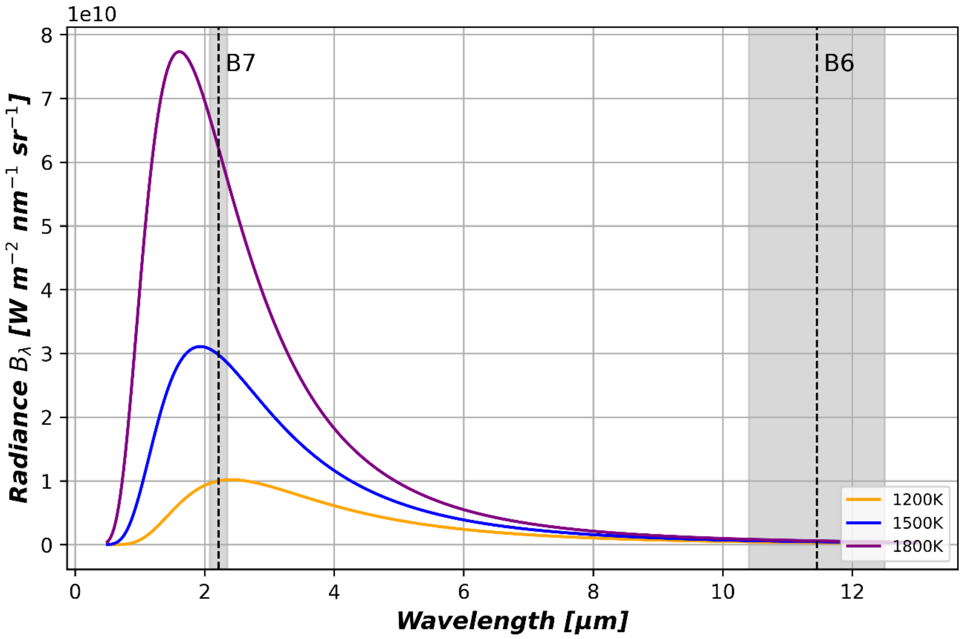

Figure S2. Plank curve for typical gas flaring temperatures and central wavelengths of Landsat 4-5 bands (B6, B7). The grey shaded areas indicate the full spectral bandwidth of each sensor band, while the vertical dashed lines represent their respective central wavelengths

ERA5-Land data were retrieved via Google Earth Engine (GEE) and are based on the climate reanalysis produced by the European Centre for Medium-Range Weather Forecasts (ECMWF) through the Copernicus Climate Change Service (C3S), providing high-resolution land surface variables from 1950 onwards (Figure S3; (3)).

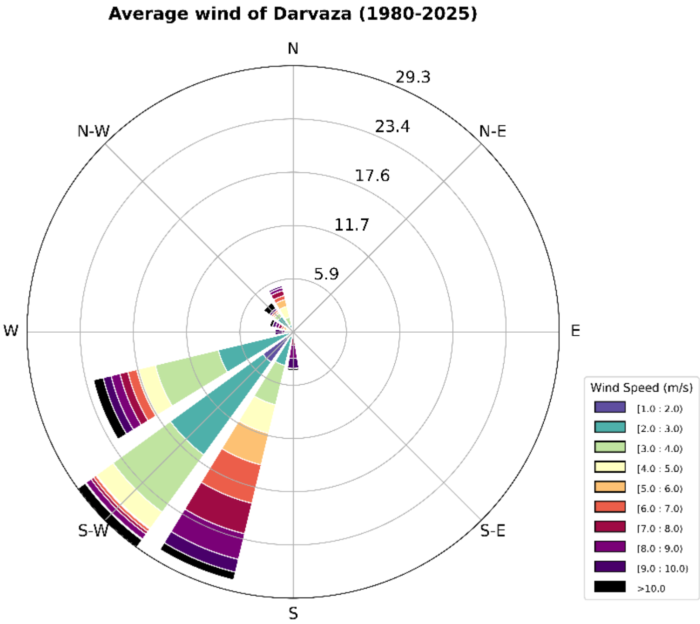

Figure S3. The average wind of the Darvaza gas crater area between 1950 and 2024 using the ERA-5 database. The numbers indicate the relative frequency of the direction of the wind.

A comparative analysis was conducted between wind speed and wind direction data derived from the GEOS-FP and ERA5 datasets (Figure S4), given the critical role of atmospheric dynamics in accurately quantifying methane emissions. While some discrepancies were observed between the two sources, these differences did not influence the emission estimates significantly.

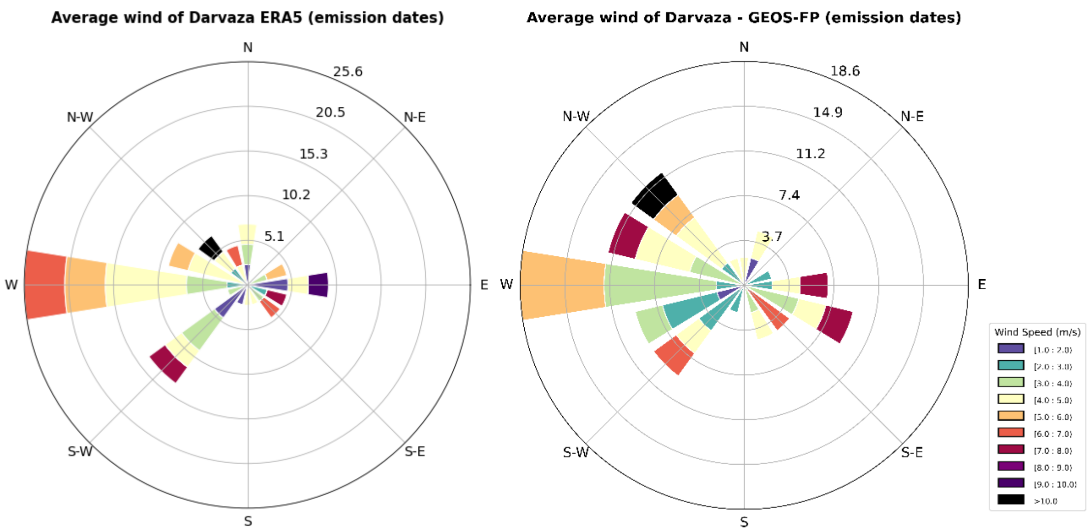

Figure S4. Comparison between wind speed and wind direction corresponding to the date of ERA-5 and GEOS-FP emissions. The numbers indicate the relative frequency of the direction of the wind.

We have analyzed a dataset that includes 9 acquisitions from the ZY-1E hyperspectral mission, 2 from GF-5, 21 from PRISMA, 9 from EnMAP, and 20 from the EMIT instrument. Specifically, 44 images showed detectable methane emissions, 8 were partially or fully cloud-covered, 5 showed no detectable plumes, and 4 were out of the instrument's swath (Table S1). Acquisitions with methane plumes detected are listed in Table S2, while those without detected emissions are listed in Table S2. All these acquisitions have been visually analyzed, and the detected plume correlated with wind direction and speed.

Table 1. Summary of total hyperspectral satellite acquisitions over Darvaza.

SENSOR	Images	Emission	Cloudy	No-emission	Out of swath
PRISMA	21	13	6	2	0
EnMAP	9	9	0	0	0
EMIT	20	14	2	0	4
ZY1-AHSI	9	6	0	3	0
GF5-AHSI	2	2	0	0	0
TOTAL	**61**	**44**	**8**	**5**	**4**

Table S2. Summary of the emissions rates from the high-resolution satellite observations. Q refers to the flux rates estimated for each plume in tonnes, and Q_err to the associated uncertainty in tonnes.

	DATE	SENSOR	Q (t/h)	Q_err (t/h)
1	2020-04-21	ZY1-AHSI	1.84	0.72
2	2021-10-09	PRISMA	0.91	0.40
3	2022-08-16	EMIT	1.06	0.50
4	2022-11-20	ZY1-AHSI	2.66	0.97
5	2023-03-29	EMIT	1.16	0.43
6	2023-04-18	EMIT	1.13	0.51
7	2023-06-13	EMIT	1.96	0.75
8	2023-06-13	ENMAP	1.36	0.53
9	2023-06-25	EMIT	1.31	0.48
10	2023-08-05	EMIT	2.23	1.03
11	2023-08-09	EMIT	1.81	0.73
12	2023-08-22	ZY1-AHSI	3.18	1.20
13	2023-08-25	EMIT	3.16	1.28
14	2023-10-16	ZY1	1.65	0.71
15	2024-02-01	EMIT	2.07	0.78
16	2024-03-26	EMIT	1.37	0.65
17	2024-03-29	ZY1-AHSI	1.16	0.50
18	2024-07-28	EMIT	0.63	0.23
19	2024-08-01	EMIT	1.12	0.44
20	2024-08-17	EMIT	0.94	0.40
21	2024-09-10	PRISMA	1.37	0.56
22	2024-09-14	ENMAP	1.75	0.68
23	2024-09-22	PRISMA	2.01	0.76
24	2024-09-22	ENMAP	1.42	0.53
25	2024-10-07	ENMAP	1.47	0.59
26	2024-10-15	ENMAP	1.22	0.42
27	2024-10-15	PRISMA	1.32	0.48
28	2024-11-02	PRISMA	0.81	0.32
29	2024-11-07	PRISMA	1.14	0.45
30	2024-11-07	ENMAP	1.26	0.49
31	2024-11-16	GF5-AHSI	2.51	1.02
32	2024-11-25	PRISMA	1.73	0.65
33	2024-12-06	PRISMA	1.14	0.40
34	2024-12-23	ENMAP	2.13	0.83
35	2025-01-10	PRISMA	1.54	0.49
36	2025-01-11	ZY1-AHSI	2.35	0.87
37	2025-01-28	PRISMA	2.31	0.92
38	2025-01-31	ENMAP	1.72	0.67
39	2025-02-14	PRISMA	0.91	0.27
40	2025-02-19	GF5-AHSI	0.82	0.22
41	2025-03-14	ENMAP	1.08	0.40
42	2025-03-15	PRISMA	1.59	0.65
43	2025-04-05	EMIT	1.14	0.49
44	2025-05-18	PRISMA	1.89	0.63

Table S3. Summary of the acquisitions with no-detected plumes from the high-resolution satellite observations and the corresponding wind speed from the GEOS-FP 1h reanalysis product.

	DATE	SATELLITE	WIND (m/s)
1	2020-08-18	PRISMA	1.57
2	2021-10-21	PRISMA	5.52
3	2023-12-23	ZY1-AHSI	4.91
4	2024-12-16	ZY1-AHSI	11.56
5	2024-12-29	ZY1-AHSI	4.88

As shown in Figure S6, our time series analysis using MODIS (2000–2019) and VIIRS (2020–2025) reveals that MODIS-derived FRP values are generally higher and exhibit greater temporal variability, whereas VIIRS data show lower, more stable values. These differences are primarily attributable to sensor-specific spatial and observational characteristics. MODIS, with its coarser 1-km resolution, integrates thermal signals over larger areas, often leading to overestimation of FRP in compact sources such as the Darvaza gas crater (~70 m in diameter). In contrast, the 375-m resolution of VIIRS allows for more spatially refined detection of localized thermal anomalies, though it typically results in lower FRP values per pixel (4). Additionally, VIIRS exhibits greater sensitivity to low-intensity flares, with a minimum detectable FRP of ~0.4 MW, compared to ~2.5–17 MW for MODIS, depending on viewing geometry (5). Wooster et al. (6) further emphasize that MODIS tends to overestimate FRP in small, hot sources due to broader pixel sampling and increased scene heterogeneity. These factors collectively explain the FRP differences observed between the two sensors at the exact location. Given these distinctions and considering that VIIRS provides higher spatial resolution and sensitivity, we consider VIIRS data to be more reliable for flaring quantification. Therefore, we focus exclusively on FRP data from 2020 to 2023, as these are the years currently available in the Global Gas Flaring Data set.

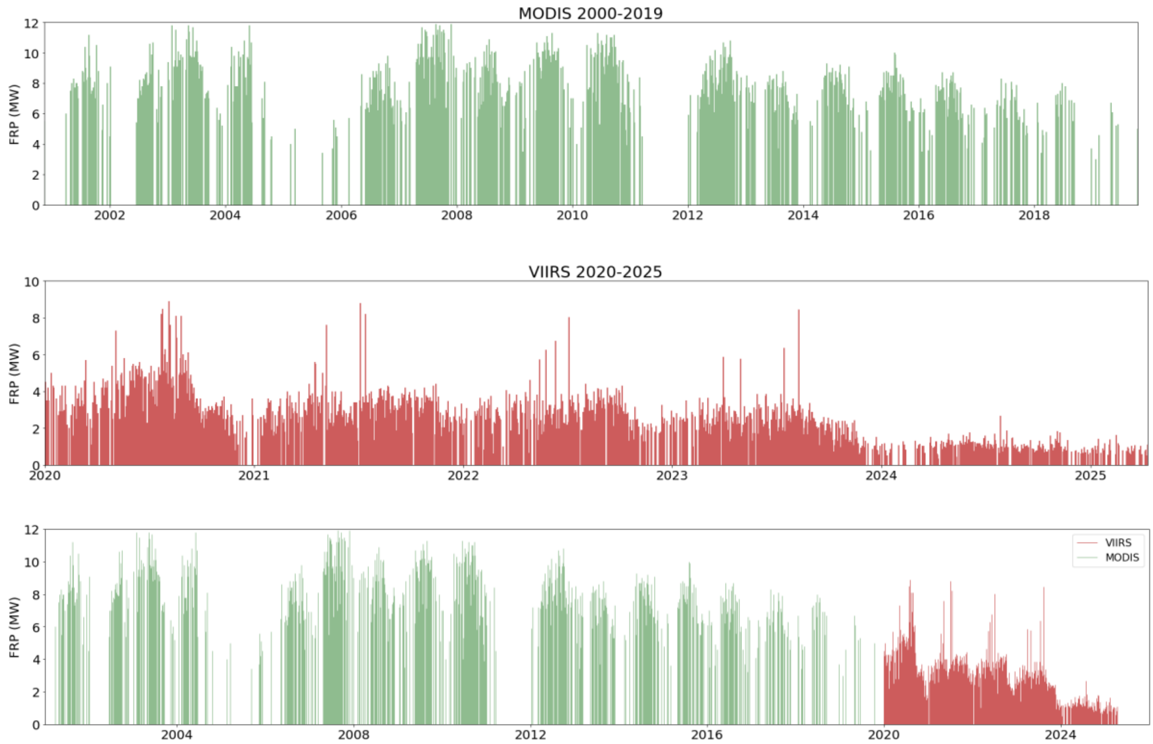

Figure S5. Flaring timeline using MODIS from year 2000 to 2019 and VIIRS (NOAA-21 and SUOMI-NPP) from 2020 to 2025. Specifically, we analyzed the Fire Radiative Power (FRP) data from both VIIRS and MODIS, which directly measure the radiant energy of fires.

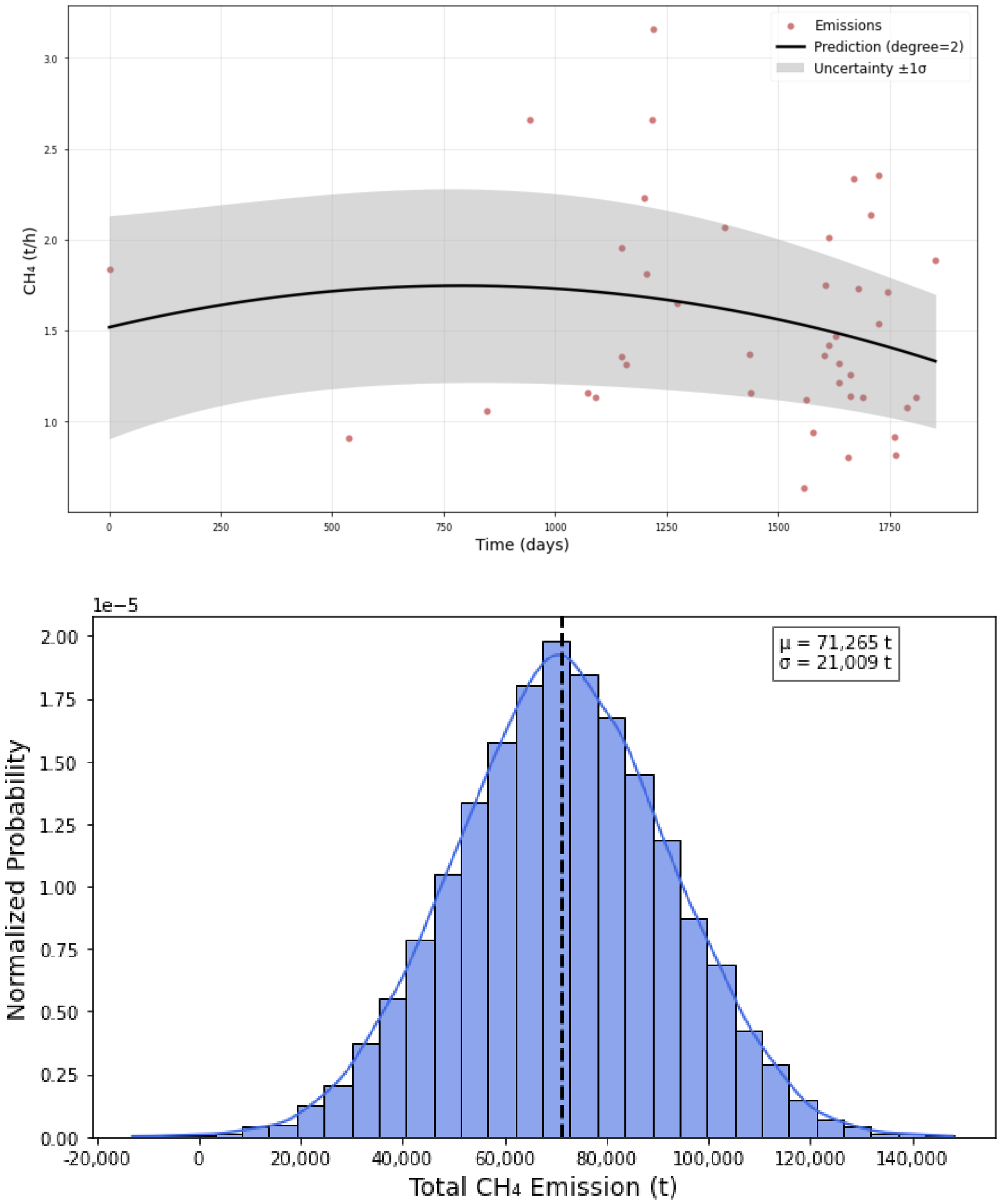

Figure S6. Total methane emissions. The upper graph presents a second-order polynomial fit to all satellites' 44 flow rate estimates. The grey-shaded region around the curve represents the uncertainty of the fit, corresponding to a coverage factor of k = 1. The lower graph displays the probability distribution function obtained by propagating both the temporal variation of the flow rate and its associated uncertainty through multivariate Monte Carlo simulations. In this process, an error correlation of 0.5 is assumed among the individual satellite observations.

Bibliography

1. T. D. Drummer, Generalized Geology of the Former Soviet Union (geo1ec). U.S. Geological Survey. https://doi.org/10.5066/P9GUL0PQ. Deposited 1998.

2. A. Caseiro, *et al.*, A Methodology for Gas Flaring Detection and Characterisation Using SLSTR. [Preprint] (2018). Available at: https://www.preprints.org/manuscript/201805.0020/v1 [Accessed 25 March 2025].

3. Copernicus Climate Change Service, ERA5-Land hourly data from 1950 to present. Copernicus Climate Change Service (C3S) Climate Data Store (CDS). https://doi.org/10.24381/CDS.E2161BAC. Deposited 2019.

4. W. Schroeder, P. Oliva, L. Giglio, I. A. Csiszar, The New VIIRS 375 m active fire detection data product: Algorithm description and initial assessment. *Remote Sensing of Environment* **143**, 85–96 (2014).

5. Y. Fu, *et al.*, Fire Detection and Fire Radiative Power in Forests and Low-Biomass Lands in Northeast Asia: MODIS versus VIIRS Fire Products. *Remote Sensing* **12**, 2870 (2020).

6. M. J. Wooster, G. Roberts, G. L. W. Perry, Y. J. Kaufman, Retrieval of biomass combustion rates and totals from fire radiative power observations: FRP derivation and calibration relationships between biomass consumption and fire radiative energy release. *J. Geophys. Res.* **110**, 2005JD006318 (2005).